Engineering Structures 318 (2024) 118745

Contents lists available at ScienceDirect

Engineering Structures

journal homepage: www.elsevier.com/locate/engstruct

Quasi-static cyclic tests of FRP-confined steel-reinforced HPFRCC circular columns

Zheng Dang [a,b,*], Peng Feng [b], Saravath Suong [b,c], Liyun Tang [a]

[a] School of Architecture and Civil Engineering, Xi'an University of Science and Technology, Xi'an 710054, China
[b] MOE Key Laboratory of Civil Engineering Safety and Durability of China, Department of Civil Engineering, Tsinghua University, Beijing 100084, China
[c] The Second Construction Co., Ltd. of China Construction Third Engineering Bureau, Wuhan 430000, China

ARTICLE INFO

Keywords:
Quasi-static cyclic test
Circular column
Compression-bending performance
Frictional force
High-performance fiber reinforced cementitious composites (HPFRCC)
Fiber-reinforced polymer (FRP)

ABSTRACT

This study presents a novel composite component comprising of steel-reinforced high-performance fiber reinforced cementitious composites (HPFRCC) circular columns confined by fiber-reinforced polymer (FRP), with the goal of improving the mechanical behavior of conventional reinforced concrete (RC) columns. Quasi-static cyclic loading tests were conducted to investigate various aspects of the column specimens, including failure phenomena, load-displacement response, sectional compression-bending performance, plastic hinge length, and lateral strain distributions in the FRP jacket, etc. A self-designed frictional force measurement device was employed to accurately measure the actual force borne by the specimen. The experiment results revealed that FRP confinement effectively improved the load-bearing capacity and deformation capacity of the specimens and delayed the deterioration of the sectional compression-bending performance. The superior tensile ductility of HPFRCC led to increased yielding displacement and peak load compared to FRP-confined concrete specimen, although this enhancement was limited. Furthermore, the peak load of the FRP-confined HPFRCC specimen increased with axial load, while the sectional compression-bending performance after the peak load remained relatively stable until approaching the collapse prevention (CP) limit state.

1. Introduction

Reinforced concrete (RC) is nowadays a very important composite material in civil engineering, providing comprehensive advantages in terms of cost efficiency, safety, constructability, and durability, while also holding great potential for future structural innovations [1]. It is commonly utilized in structural lateral force-resisting members, such as RC bridge piers, frame columns, and shear walls, and the mechanical behaviors of RC members directly affect the seismic performance of the structure [2]. However, the inherent brittleness of concrete makes it prone to cracking and fracturing under external loads or environmental influences. This leads to a tensile softening behavior in the stress-strain relationship after cracking, as shown by curve (a) in Fig. 1. As a result, a chain reaction of damage evolution occurs in RC members, starting with stress concentration on longitudinal reinforcements, followed by loss of confinement effect on transverse reinforcements, and ultimately resulting in concrete crushing and a decrease in the load-bearing capacity of the member. Additionally, the concrete primarily responsible for bearing compressive stress in RC member exhibits compression softening behavior after reaching peak strength, as shown by curve (c) in Fig. 1. This behavior restricts significant improvements in compressive-bending performance, including load-bearing capacity and deformation capacity. Consequently, the potential for enhancing the mechanical behavior of RC members using conventional materials is considered to be rather limited.

Research has confirmed that fiber reinforcement is an effective method to improve the ductility of concrete [3,4]. According to the principles of micromechanics, the tailored short fibers with high elastic modulus and tiny diameter are added into the cement mortar with a specific mix proportion to meet the interface properties between fibers and mortar matrix. This can result in the development of tensile strain hardening behavior in fiber-reinforced cementitious composites, as shown by curve (b) in Fig. 1. Such materials are commonly referred to as high-performance fiber-reinforced cementitious composites (HPFRCC) [5]. Several experiments have been conducted to investigate the influence of HPFRCC on the seismic performance of RC columns. Cho et al.

* Corresponding author at: School of Architecture and Civil Engineering, Xi'an University of Science and Technology, Xi'an 710054, China.
E-mail addresses: dangzheng@xust.edu.cn (Z. Dang), fengpeng@tsinghua.edu.cn (P. Feng), saravathsuong.cscec32@gmail.com (S. Suong), tangly@xust.edu.cn (L. Tang).

https://doi.org/10.1016/j.engstruct.2024.118745
Received 1 July 2023; Received in revised form 11 July 2024; Accepted 5 August 2024
Available online 17 August 2024

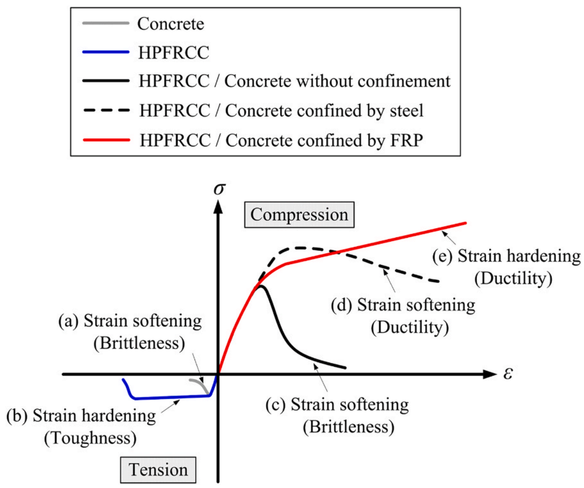

Fig. 1. Axial compressive and tensile behaviors of HPFRCC and concrete.

[6] found that RC composite columns, strengthened in the plastic hinge region using HPFRCC, not only improved lateral load and deformation capacity but also reduced bending and shear cracks in the flexural critical region of the columns. Xu et al. [7] discovered that replacing the concrete in the column with HPFRCC could avoid premature flexure-shear failure, prevent cover splitting, maintain structural integrity, and partially replace stirrups. The study by Li et al. [8] revealed that the cyclic performance of RC columns repaired with HPFRCC was better. By increasing the repair height beyond the plastic hinge zone, both load-bearing capacity and ductility of the columns were slightly improved.

To effectively utilize HPFRCC in seismic members, it is essential to understand the mechanism and behavior of HPFRCC under tension and compression. Fischer et al. [9,10] discovered that the most direct contribution of HPFRCC was to maximize the load-bearing capacity and energy dissipation capacity of steel reinforcements. This was achieved through strain coordination between HPFRCC and steel reinforcements due to the strain hardening behavior of HPFRCC, which maintained the integrity and synergy of steel-reinforced HPFRCC composites. Correspondingly, Kesner and Billington [11] also found that the damage of steel plate occurred after tensile softening of HPFRCC, with the post-peak load-deformation hysteresis response being dependent on the steel reinforcements. Additionally, Kesner et al. [12,13] observed that compression softening of HPFRCC could lead to the formation of local cracks, resulting in premature failure of the tensile strain hardening behavior at cracks. Therefore, it is crucial to preserve the strain-hardening behavior of HPFRCC under both tensile and compressive loading to fully exploit its performance advantages.

On the other hand, it is well known that the lateral confinement method can significantly enhance the ultimate compressive strength and deformation capacity of cement-based materials [14–17]. Fiber-reinforced polymer (FRP) is a typical confining material that, owing to its linear elastic properties, can generate continuously increasing lateral confinement pressure with the passive expansion of cement-based materials. This allows confined cement-based materials to exhibit secondary hardening behavior under axial compression, as shown by curve (e) in Fig. 1 [18,19]. This behavior differs from the strain softening behavior of cement-based materials confined by steel, as shown by curve (d) in Fig. 1. Therefore, FRP plays a crucial role in reinforcing and strengthening RC piers and columns [20–23]. Previous experimental studies by the authors of this paper [24] and others [25–29] have demonstrated that FRP-confined HPFRCC cylinders with sufficient lateral confinement can exhibit typical axial compression hardening behavior.

Therefore, a novel FRP-confined steel-reinforced HPFRCC composite column with a circular cross-section was proposed in this study. The combination of high-ductility HPFRCC with steel reinforcement was aimed at maintaining the integrity and synergy of the composite column. Moreover, the FRP confinement jacket was used to achieve the axial compression strengthening behavior of HPFRCC and mitigate the adverse effects of compressive damage on its tensile strain hardening property during cyclic loading. This research will primarily focus on examining the compression-bending performance of the column cross-section under quasi-static cyclic loading, while also exploring the influence of FRP confinement, high-ductility HPFRCC, and axial load ratios on the seismic behavior of the column specimens. The experimental program chosen for this study aimed to minimize interference factors and ensure ideal force conditions, prioritizing experimental rigor over practical application considerations.

2. Experimental program

2.1. Test specimens

The engineering prototype used in this study was a ground floor column from a multi-story frame structure, measuring 5400 mm in height and 600 mm in diameter. In general, the distance from the foundation to the inflection point of the column bending moment was around half of the column height. As a result, the lower half of the columns were designed as test specimens at a scale of 1:2.5, as shown in Fig. 2. These column specimens consisted of a bottom beam, a cantilever column with a circular cross-section, and a cube loading end. The diameter D of the column specimen was 240 mm, and the thickness c of the concrete cover was 10 mm. The height H of the column specimen was 905 mm, and the horizontal loading point was located at the mid-height of the loading end, 175 mm from the top. The actual equivalent height H' of the column specimen was 1080 mm, corresponding to a shear span ratio of 4.5.

A total of four column specimens with identical geometric dimensions and reinforcement configurations were designed and produced for this test. Three of the specimens were made of HPFRCC with a fiber volume content of 2 % (labeled as ‘H’), while the fourth specimen was composed of normal concrete (labeled as ‘N’) and served as the control group. To investigate the effect of FRP confinement on column behavior, three specimens were confined with seven-layers carbon fiber-reinforced polymer (CFRP) sheets (labeled as ‘C7’), but the other specimen was left unconfined (labeled as ‘U0’). In addition, in order to evaluate the influence of axial loads, the specimens were subjected to two different axial loads of 600 kN and 1200 kN, corresponding to the test axial load ratios of 0.2 and 0.4 (labeled as ‘0.2’ and ‘0.4’, respectively). Thus, the naming convention for the specimens followed the format: Cement-based material - confinement level - axial load ratio. Detailed specimen information can be found in Fig. 2 and Table 1.

In this test, in order to compare the seismic behavior of specimens, it is important to minimize the difference in compressive strength and elastic modulus between HPFRCC and normal concrete as much as possible. Thus, the mixture proportions of the two cement-based materials were made almost identical except for the addition of fibers and coarse aggregates, as shown in Table 2. The cement was P.O. 42.5 ordinary Portland cement, the fly ash (FA) was Grade I, and the fine aggregate was fine quartz sand with a maximum particle size of 0.42 mm. HPFRCC did not contain coarse aggregate, but normal concrete contained gravel coarse aggregate with a maximum particle size of 20 mm. Due to the small particle size of aggregate and the large volume of cement paste, cement-based materials may exhibit volume instability. Expansion agents were employed to reduce the volume shrinkage of the cement matrix after setting and hardening. A polycarboxylate superplasticizer with a solid content of 20 % was utilized as a high-range water-reducing admixture. The mixing water was tap water, and the water-cementitious material ratio (W/C) was adjusted to 0.3. The short fibers used were REC 15 × 12 polyvinyl alcohol (PVA) fibres with a fiber

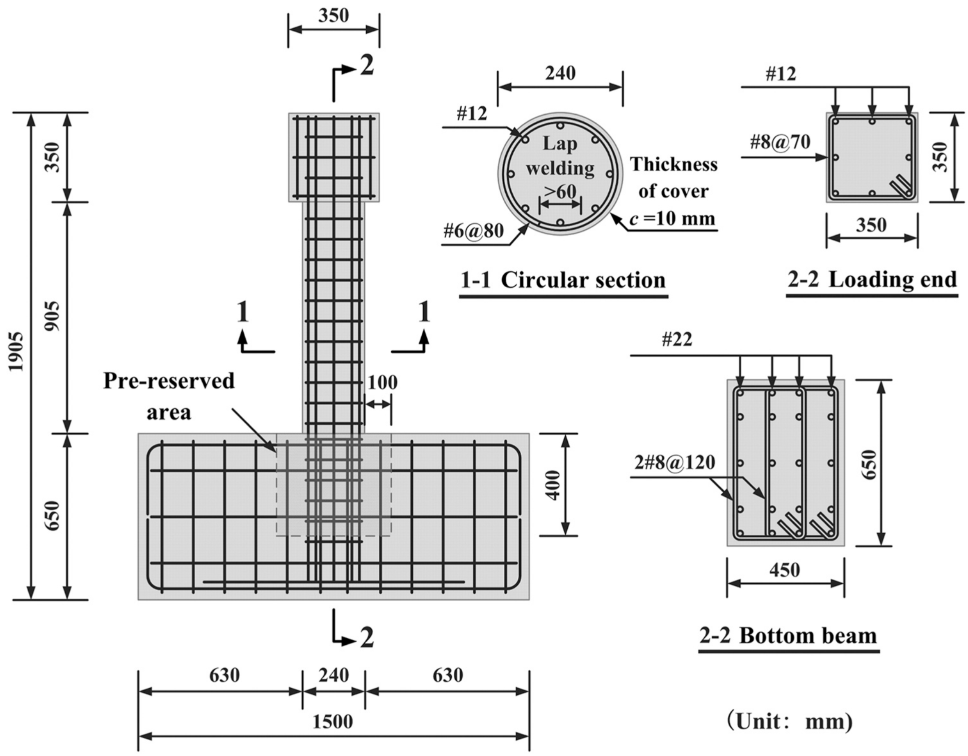

Fig. 2. Dimension and reinforcement details of test specimens.

Table 1
Test matrix of the column specimens.

Specimen	Cement-based material	Layers of CFRP sheets	Axial load ratio	Axial load P (kN)	Height of confinement zone (mm)	Longitudinal bars	Circular hoops
H-U0 −0.2	HPFRCC	0	0.2	600	—	8#12	#6@80
H-C7 −0.2	HPFRCC	7	0.2	600	500		
H-C7 −0.4	HPFRCC	7	0.4	1200	500		
N-C7 −0.2	Normal concrete	7	0.2	600	500		

Table 2
Mix proportions of HPFRCC and concrete by weight.

Raw materials	Cement	FA	Expansion agent	Quartz sand	Water	Superplasticizer	Coarse aggregate	PVA fiber
HPFRCC	1.0	1.0	0.20	0.72	0.60	0.005	—	0.044
Normal concrete	1.0	1.0	0.20	0.72	0.60	0.0025	1.0	—

volume concentration of 2.0 % from Kuraray Corp. in Japan [24]. During casting, the flowability and passing ability of fresh mortar mixtures in narrow gaps between steel reinforcements were improved by limiting the maximum particle size of coarse aggregates, using polycarboxylate superplasticizer and adding fly ash fillers [30,31].

The steel reinforcement detail was consistent across all column specimens. Longitudinal reinforcements in the column were made up of eight 12-mm-diameter steel bars (8#12) uniformly arranged around the circumference of the section, resulting in a design reinforcement ratio ρ_s of 2.0 %. These longitudinal reinforcements extended vertically through the entire column, connecting to both the bottom beam and the top loading end. Stirrups were composed of 6-mm-diameter steel bars spaced 80 mm apart (#6@80), welded into single-sided overlapping circular hoops with a full welded length of 60 mm. The column specimens had a volume stirrup ratio ρ_{sv} of 0.68 %, which allowed the confinement effect of the circular hoops to be neglected [32]. Besides, the bottom beam of the specimen was constructed using concrete. To prevent the formation of construction joints at the base of the column following the initial concrete setting, HPFRCC or normal concrete was poured vertically along the column, as well as the adjacent pre-reserved area at the top of the bottom beam. After pouring the HPFRCC and concrete, the speciemns must be cured for at least 28 days.

The gaps at the interface between the confining material and the core column, caused by volume shrinkage due to cementitious material hydration, can significantly impair the confinement effect of FRP. Therefore, the experiment adopted a manual wrapping of carbon fiber-reinforced polymer (CFRP) sheets around the hardened cement-based material, instead of pouring the cement-based material straight into CFRP tubes. During wrapping CFRP sheets, epoxy resin was uniformly applied on CFRP sheets and cured in a dry and warm environment for at least 7 days. For research purposes, seven layers of CFRP sheets were used to provide sufficient lateral confinement for HPFRCC core column, achieving an actual confinement ratio, $f_{l,a}/f'_{co}$ greater than 0.4 [24]. This allowed the axial compression property of the FRP-confined HPFRCC to exhibit standard post-yield strengthening behavior. Considering the constructive feasibility, a strategy of wrapping CFRP sheets with reliable bonding was implemented [33]. Each confined specimen was enveloped with three CFRP sheets arranged in a continuous head-to-tail sequence, as illustrated in Fig. 3. To ensure a secure lapping and consistent thickness, each CFRP sheet was overlapped between the start points (SP), forming an arc approximately 250 mm in length with a circular angle of 120°. The carbon fibers were oriented parallel to the wrapping direction of the CFRP sheets at a 0° angle to the cross-section of the column. The CFRP wrapping area extended 500 mm above the base of the column, roughly twice the diameter of the column. In order not to affect the stiffness of the column, a 10 mm gap was left between the bottom edge of the CFRP sheets and the base of the column.

2.2. Material properties

2.2.1. Steel reinforcement

The material properties of steel reinforcement were examined according to GB/T 228.1–2021 [34]. The tensile test was conducted using a 300 kN electro-hydraulic servo universal testing machine, and the loading speed was controlled at 6.0 kN/min. Two types of steel reinforcement were examined, consisting of HRB400 grade steel bar for longitudinal bars and CRB600H grade steel bar with a single-sided welded length of 60 mm for circular hoops. Three specimens of each type of steel reinforcement were tested, and the average values of the test results are presented in Table 3.

2.2.2. CFRP sheet

The tensile tests of the CFRP flat coupons were conducted according to ASTM D3039 [35] and GB/T 3354–2014 [36]. Six specimens with a length of 230 mm and a width of 25 mm were tested. The CFRP flat coupons were composed of three layers of sheets, each with a nominal thickness of 0.111 mm, and the fiber direction was parallel along the length of the coupons. The tensile test was performed using a 300 kN electro-hydraulic servo universal testing machine, with a loading speed of 1.5 mm/min. The axial strain was calculated using the average value of the unidirectional strain gauges (with a gauge length of 10 mm) positioned symmetrically at the midpoint of the plate on both sides, while the axial stress was calculated by the nominal thickness of CFRP flat coupons [37]. The tensile properties of the CFRP were determined from the average of six specimens, and the tensile properties are shown in Table 4.

2.2.3. HPFRCC and concrete

The compressive strength of HPFRCC and normal concrete were tested according to GB/T 50081–2019 [38]. The compression test was conducted using a 2000 kN testing machine, with a loading speed of 1.0 MPa/s. The axial compression specimens consisted of cubes with a side length of 150 mm, cubes with a side length of 100 mm, and cylinders with a diameter of 100 mm and a height of 200 mm. The

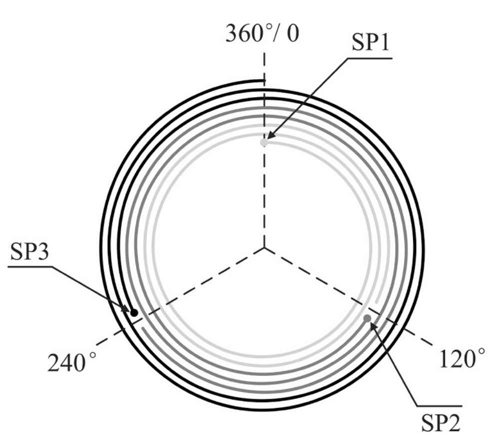

Fig. 3. Wrapping strategy of CFRP sheets.

compressive strength of HPFRCC and normal concrete are shown in Table 5.

The size conversion factor for HPFRCC, determined from the ratio of the compressive strength of cubes with the side length of 150 mm and 100 mm (f_{cu-150}/f_{cu-100}) at the age of 35 days, is smaller at 0.886, while that of normal concrete is 0.920. Based on axial compression tests on cylinders at the age of 84 days, the average elastic modulus for HPFRCC and concrete are 21898 MPa and 28379 MPa respectively, and the lateral strains at peak compressive strength are 1500 $\mu\varepsilon$ and 706 $\mu\varepsilon$. In this test, the actual strength of the member was determined by the compressive strength of a cylinder with a diameter of 150 mm (f'_{c-150}). It was assumed that the size conversion factor of the cylinder (f'_{c-150}/f'_{c-100}) is equivalent to that of the cube (f_{cu-150}/f_{cu-100}) [38]. Thus, the compressive strength of the column specimen at the test age of 84 days is considered as 66.2 MPa (=74.7 MPa×0.886) for HPFRCC and 64.5 MPa (=70.1 MPa×0.920) for normal concrete, respectively.

The tensile properties of HPFRCC and normal concrete were tested using five rectangular flat plates with a geometric dimension of 200 mm × 100 mm × 20 mm, and the test results are shown in Table 6. The tensile tests were conducted using a 250 kN dynamic material testing machine with a loading speed of 0.15 mm/min, and a measuring gauge length of 50 mm. The test results indicated that normal concrete had a very low toughness after cracking, whereas HPFRCC exhibited obvious strain hardening behaviors. HPFRCC had an average ultimate tensile strain of 1.11 % and fracture energy of 2.47 kJ/m^2, which were 65 times and more than 20 times higher than those of normal concrete, respectively.

2.3. Test setup and procedures

The quasi-static cyclic test setup, shown in Fig. 4, involved a 2000 kN hydraulic jack for vertical compression load and an electro-hydraulic servo actuator with a load range of 1000 kN and a displacement range of ± 300 mm for horizontal cyclic load. This test setup allowed for the application of both positive and negative forces and displacements by pushing and pulling the actuator, respectively. The bottom beam of the specimen was fixed to the laboratory rigid floor using ground anchor bolts and rigid beams, while anti-slip jacks prevented sliding of the specimen along the loading direction. The horizontal loading point located at the center of the loading end of the column was linked to the horizontal actuator by a connector with a one-way hinge, and the vertical jack was fastened to support with a set of rigid rollers mounted upside down on the reaction beam. To measure the frictional force generated between the roller support and the reaction beam and eliminate the interference of frictional force on the restoring force of the specimen, a specially designed device was placed between the loading end of the specimen and the vertical jack.

The horizontal cyclic loading was applied after the axial load being applied at the top of the column. The loading history was divided into two stages. The first stage (Phase I) is before the drift δ reaches ± 1.00 %, with small displacement amplitude and one cycle per level of displacement. The second stage (Phase II) is after the drift δ reaches and exceeds ± 1.00 %, with an increase in displacement amplitude and each level of displacement cycled twice, as shown in Fig. 5. The horizontal loading was controlled by the drift at the top of the column, which served as a displacement increment, unaffected by variances in yield displacement among different specimens. The drift values under different limit states were determined by building standards [39] and [40]. The loading was stopped when the horizontal load of the specimen dropped to 20 % of the peak load or the specimen could no longer stably resist the vertical load.

2.4. Test instrumentations and strain layout

Fig. 6 shows the arrangement of 14 Linear Variable Displacement

Table 3
Mechanical properties of steel reinforcements.

Brand of steel	Number of specimens	Diameter d (mm)	Yield strength f_y (MPa)	Ultimate strength f_u (MPa)	Young's modulus E_s ($\times 10^5$ MPa)	Percentage elongation after fracture A (%)
HRB400	3	12	419.8	582.5	1.94	24.7
CRB600H (Without welds)	3	6	615.0	689.5	2.08	15.3
CRB600H * (With welds)	3	6	—	509.1	—	—

Note: * The ultimate strength of the circular hoops in the column specimens was determined using the tensile test results of CRB600H grade steel bars with 60 mm-long welds, and the stirrup characteristic value was calculated to be 0.07.

Table 4
Tensile properties of CFRP flat coupons.

Number of specimens	Elastic modulus E_{frp} (GPa)		Tensile strength f_{frp} (MPa)		Ultimate tensile strain ε_{frp} (%)	
	Ave.	S. D.	Ave.	S. D.	Ave.	S. D.
6	237.4	8.4	4367	220	1.83	0.12

Note: "Ave." stands for "Average", and "S. D." stands for "Standard Deviation".

Transformers (LVDTs) for each specimen. LVDT-1 and LVDT-2 are mounted horizontally at the center of the loading end at the top of the column (i.e. 1080 mm from the column base) to measure horizontal displacement at the top of the specimen, while LVDT-3 is installed horizontally at a height of 550 mm from the column base to measure horizontal displacements caused by the deformations of potential plastic hinge zone. LVDT-9 and LVDT-10, LVDT-7 and LVDT-8, and LVDT-5 and LVDT-6 are vertically installed along both sides of the column to measure average sectional curvature at various heights. LVDT-13 and LVDT-14 are diagonally installed at 550 mm height on the back of the specimen to measure shear deformation. LVDT-4 is installed horizontally at the end of the bottom beam to monitor the rigid body sliding of the specimen. LVDT-11 and LVDT-12 are vertically installed at the bottom of the loading end to measure axial deformation. To cover a wide cracked area, the measuring points of the vertical and oblique LVDTs located at the column base are set at the top surface of the bottom beam and regarded as fixed points.

Strain gauges were used to measure the local strain of the longitudinal reinforcement, circular hoop, and CFRP jackets. The longitudinal bars were monitored at five different heights, including 75 mm below the upper surface of the bottom beam, and heights of 25 mm (Section-1), 100 mm (Section-2), 250 mm (Section-3) and 450 mm (Section-4) above it, as shown in Fig. 7. The circular hoops were monitored at heights of 120 mm (near Section-2) and 280 mm (near Section-3) above the column base, with three strain gauges dispersed at 90° intervals along the circumference, excluding the weld area, as shown in Fig. 7 **(a, b)**. Similarly, the CFRP jackets were monitored at Section-1, Section-2, and Section-3, with strain gauges arranged equally at eight positions along the circumference of the column. The strain gauges were labeled based on the rule of 'measurement point position - section location - strain gauge direction' [41], with specific positions denoted by letters from 'a' to 'h' for circular hoops and from 'A' to 'H' for CFRP jackets. Vertical strain gauges were marked with 'V' for CFRP and 'v' for steel rebar, while horizontal strain gauges were marked with 'H' for CFRP and 'h' for steel rebar.

3. Experimental results and discussions

3.1. Test observations

Fig. 8 illustrates the failure phenomena observed during testing of the four column specimens. Specimen H-U0–0.2, an unconfined HPFRCC column, no cracking was observed until the top horizontal drift (δ) of the column reached 1/550. However, once the longitudinal bars yielded under compression, the number of cracks increased rapidly. Upon reaching the peak load with a drift of 1/50, vertical cracks appeared on the compressive side of the column base. Subsequently, at a drift of 1/25, the longitudinal bars buckled and the HPFRCC cover crushed, leading to failure dominated by compression and bending (Fig. 8**a (1)**). After removal of the HPFRCC, severe buckling and fracture of the longitudinal bars were observed (Fig. 8**a (2)**). Additionally, Specimens H-C7–0.2, H-C7–0.4, and N-C7–0.2 were CFRP-confined columns, which rendered direct observation and comparison of crack development in HPFRCC or concrete difficult. No lateral fracture of

Table 5
Compressive properties and strength conversion of HPFRCC and concrete.

Cement-based material	Age (d)	Number of specimens	Cube strength $f_{cu\text{-}150}$ (MPa)		Cube strength $f_{cu\text{-}100}$ (MPa)		Cylinder strength f'_{c100} (MPa)		Size conversion factor $f_{cu\text{-}150}$ / $f_{cu\text{-}100}$
			Ave.	S. D.	Ave.	S. D.	Ave.	S. D.	
HPFRCC	35	3	58.5	5.6	66.0	1.4	—	—	0.886
	84	2	—	—	—	—	74.7	8.6	
Normal concrete	35	3	56.0	3.4	60.9	1.0	—	—	0.920
	84	2	—	—	—	—	70.1	0.8	

Table 6
Tensile properties of HPFRCC and concrete.

Cement-based material	Number of specimens	Cracking strength (MPa)	Cracking strain (%)	Elastic modulus (GPa)	Peak strength (MPa)	Peak strain (%)	Ultimate strength (MPa)	Ultimate tensile strain (%)	Fracture energy (kJ/m^2)
HPFRCC	5	3.09	0.018	28.1	3.48	0.457	2.48	1.11	2.47
Normal concrete	3 #	2.58	0.008	35.7	—	—	—	—	0.11

Note: # The tensile properties of normal concrete were determined by averaging the results of three specimens with similar tensile properties.

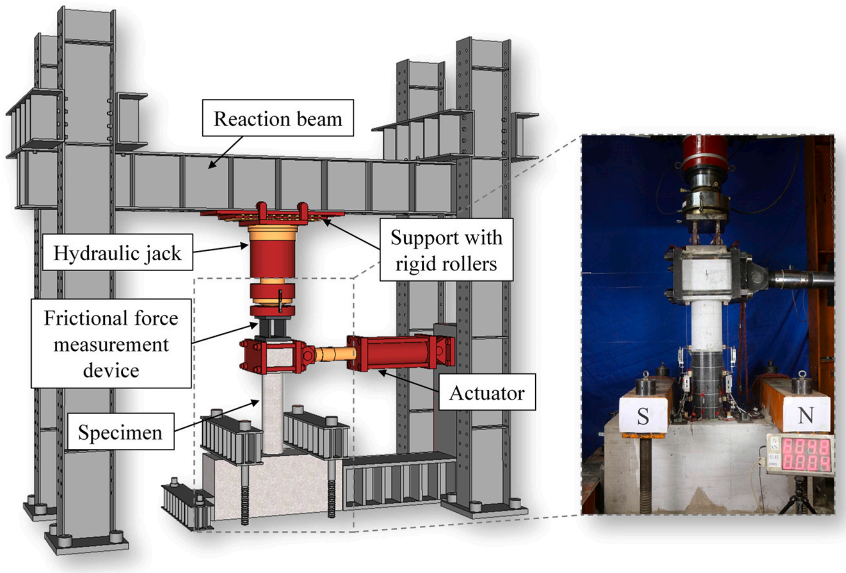

Fig. 4. Test setup.

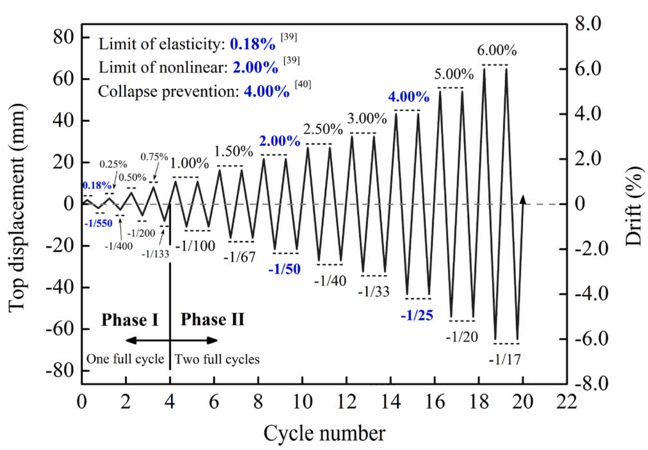

Fig. 5. Cyclic loading scheme.

CFRP occurred during loading in any of the three specimens. The ultimate failure of all three columns was attributed to the loss of compression-bending performance in the column section, resulting in flexural-dominated failure. However, there were differences among the specimens. Specimens H-C7–0.2 and H-C7–0.4 appeared only a few horizontal cracks in the CFRP at the column base and 100 mm above it (Fig. 8**b (1)** and Fig. 8**c (1)**). In contrast, specimen N-C7–0.2 had more and wider horizontal cracks in the CFRP within a range of 200 mm above the column base (Fig. 8**d (1)**). These cracks roughly corresponded to the positions of cracks observed on the HPFRCC or concrete after removing the CFRP jackets. Specimens H-C7–0.2 and H-C7–0.4 showed fewer cracks and no significant spalling or crushing of HPFRCC (Fig. 8**b (2)** and Fig. 8**c (2)**), while specimen N-C7–0.2 had more cracks and minor spalling of concrete (Fig. 8**d (2)**). Upon removal of the HPFRCC or concrete, a slight buckling of the longitudinal bars at the bottom of all three specimens were observed (Fig. 8**b (3)**, 8**c (3)**, 8**d (3)**), which can be attributed to the lateral confinement provided by the CFRP.

3.2. Measurement of frictional force

The test loading program, similar to the one shown in Fig. 4, has been widely used for testing the cyclic behavior of members. Nevertheless, the accuracy of measuring the restoring force of specimens may be affected by the presence of frictional force in an unmodified test program [42–44]. In order to address this problem, a specialized device was created for measuring the frictional force in this test, as demonstrated in

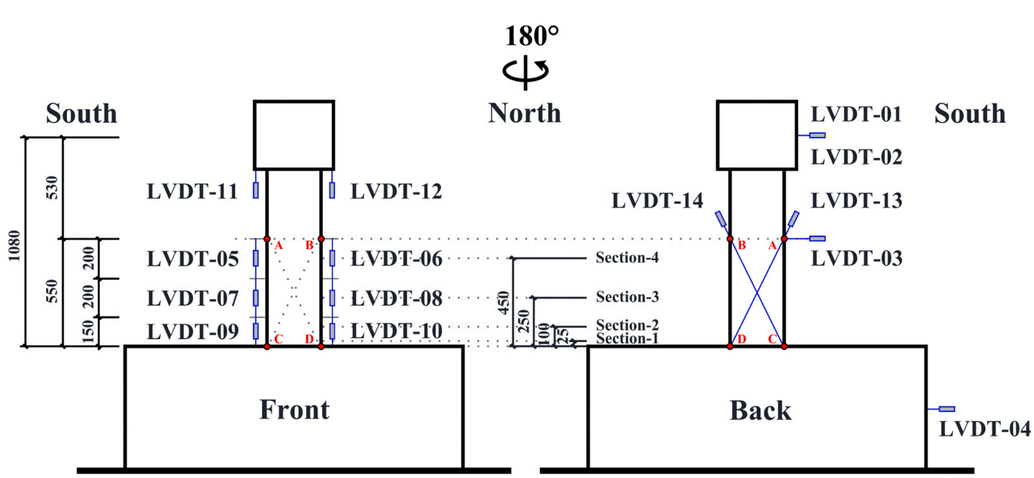

Fig. 6. Arrangement of LVDTs.

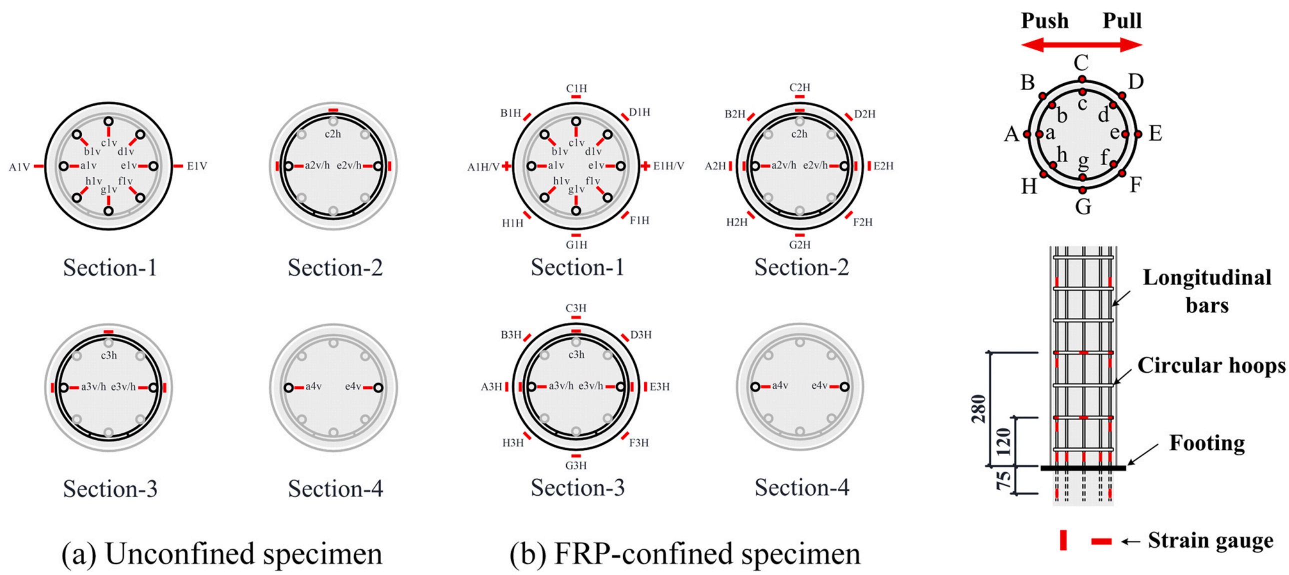

Fig. 7. Layout of strain gauges.

Fig. 9.

Fig. 9 illustrate the fundamental principle of the frictional force measurement device. As the loading end of the specimen is horizontally displaced, a frictional force occurs between the vertical jack and the reaction beam. This force is applied to the top of the specimen as static friction, equal in magnitude but opposite in direction to the horizontal actuator. Consequently, the total horizontal force exerted by the actuator is the sum of the restoring force of the specimen and the frictional force. To measure the static frictional force, a set of upright deformable steel plates is used in the frictional force measurement device, positioned between the jack and the specimen. As shown in Fig. 9**b**, applying a pair of equal horizontal shear forces Q in opposite directions on the upright steel plate led to the generation of a bending moment $M = Q \bullet h$ between the sections separated by a distance h. This bending moment could induce a variation in strain across the thickness of the steel plate. By measuring the resulting strain variation, the shear forces Q could be indirectly calculated, enabling the determination of the frictional force. The formula for this calculation was provided as follows [45]:

$$Q = \frac{M}{h} = \frac{Eat^3(\varepsilon_1 - \varepsilon_2 - \varepsilon_3 + \varepsilon_4)}{12ht} \tag{1}$$

where t is the section width of the deformable steel plate, a is the section length of the steel plate and E is the elastic modulus of the steel. The ε_1, ε_2, ε_3, and ε_4 are the measured readings of the four vertical strain gauges arranged symmetrically on the steel plate.

Considering the non-uniform deformation of the steel plate, four sets of strain gauges were symmetrically positioned on the two pieces of deformable steel plates in the frictional force measurement device, as shown in Fig. 9**a**. The total frictional force, f was then determined by averaging the shear force values measured by these four sets of strain gauge, as shown in Eq. 2:

$$f = Q \bullet n = \frac{Q_1 + Q_2 + Q_3 + Q_4}{4} \bullet n \tag{2}$$

where n is the number of deformable steel plates, in this test $n = 2$.

In reality, the relative displacement of the horizontal rigid plates on the frictional force measurement device could affect the vertical strains of the upright deformable steel plate due to shear-induced bending moment, axial force, and bending moment caused by eccentric compression. However, based on Eq. 1, the shear force due to eccentric compression was found to be zero, and the shear force from the axial force was negligible. Hence, the influence of the axial force could be disregarded.

Additionally, the movement of the loading end of the cantilever column specimen causes tilting of the frictional force measurement device (Fig. 9**c**), leading to a specific tilt angle in the measured frictional force-displacement hysteresis curve. This tilt angle necessitates correction. The true horizontal frictional force could be determined by decomposing the vertical axial force and the horizontal frictional force acting on the tilted frictional force measurement device, as shown in the Eq. 3:

$$f = \frac{P\sin\theta + f^*}{\cos\theta} \tag{3}$$

where f^* was the uncorrected measured frictional force and f was the corrected frictional force; $\sin\theta \approx \sin\theta' = \frac{\Delta}{\sqrt{\Delta^2+H^2}}$, $\cos\theta \approx \cos\theta' = \frac{H'}{\sqrt{\Delta^2+H^2}}$.

Fig. 10 displays the hysteresis curve of frictional force versus top displacement, using specimen H-U0–0.2 as an example. This demonstrates the importance of correcting the incline angle in frictional force measurements. The hysteresis curve exhibits an overall incline before correction. However, upon application of the correction, the hysteresis curve becomes horizontal and assumes a regular behavior at the starting position of reverse loading. Throughout cyclic loading, the hysteresis curve exhibits a roughly parallelogram shape, implying steady frictional force. Variations in frictional force post-reverse loading are primarily due to the instability of axial force, with a general trend of higher axial loads leading to increased frictional force.

3.3. Force-displacement responses

The hysteresis responses for lateral force versus top displacement of four column specimens are shown in Fig. 11. The black solid line represents the force-displacement relationship curve with frictional force eliminated. In this test, the cracking state was identified by visible cracks in the cement matrix, while the yield state was determined mainly by measuring the strain on the outermost longitudinal bars of the specimen reaching yield. The peak state was determined by the horizontal load reaching its maximum, and the ultimate state was defined as the load dropping to 85 % of the peak load. The corresponding values of load and displacement for the cracking, yielding, peak, and ultimate states are presented in Table 7 and Table 8.

Due to the triangular bending moment distribution along the height of the cantilevered column, where the bending moment is largest at the bottom and decreases to zero at the top, the load-bearing capacity and

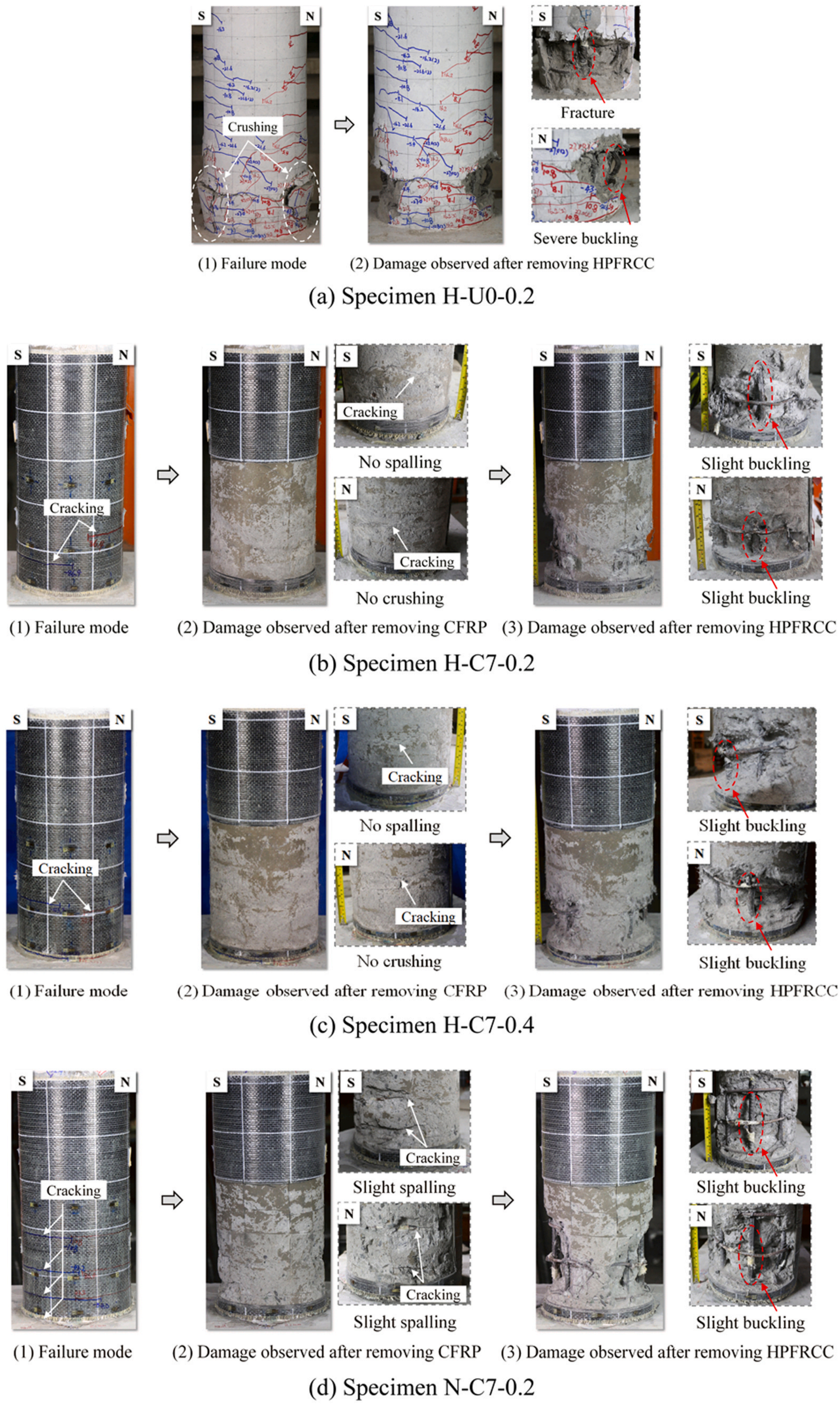

Fig. 8. Damage of columns after testing.

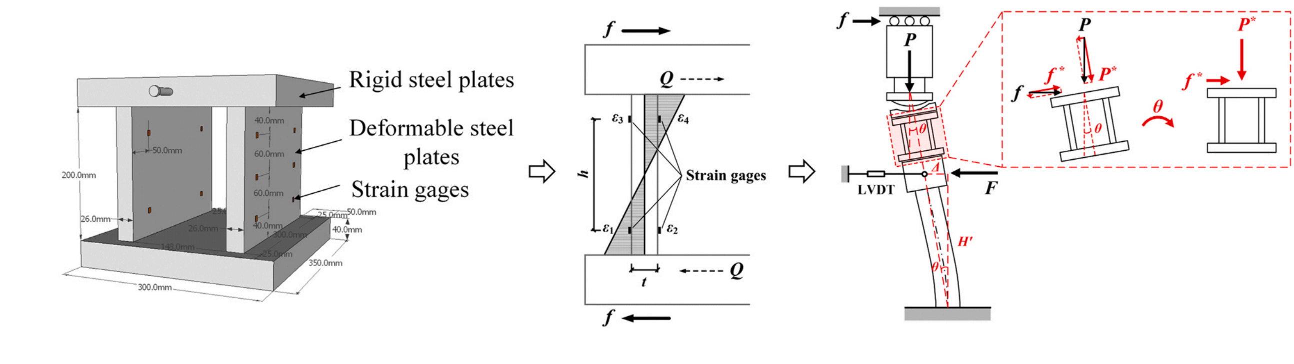

(a) Frictional force measurement device (b) Force diagram (c) Inclination correction

Fig. 9. Measurement of frictional force.

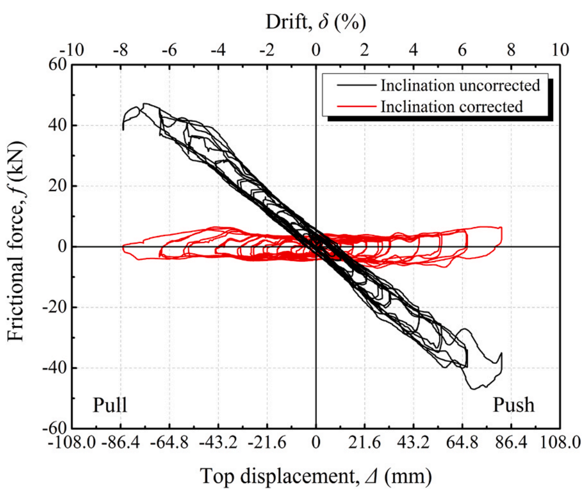

Fig. 10. Frictional force vs top displacement hysteresis curves.

deformation capacity of the column is mainly determined by the compression-bending performance of the critical section at the column base. Compared to specimen H-U0–0.2, specimen H-C7–0.2 shows an average increase of 10 % in yielding load and 14 % in peak load, as well as an average increase of 9 % in yielding displacement and 7 % in ultimate displacement. These improvements are attributed to the confinement effect of CFRP jackets, which enhanced the compression strength and deformation capacity of HPFRCC. Moreover, with an increase in axial load, specimen H-C7–0.4 shows an average decrease of 36 % in yield displacement compared to specimen H-C7–0.2, along with an average increase of 27 % in peak load and an average 19 % decrease in displacement at peak load. Furthermore, when compared to specimen H-C7–0.2, specimen N-C7–0.2 maintains the same yielding load but has an average decrease of 8 % in yielding displacement, likely due to the higher elastic modulus of concrete. The peak load of specimen N-C7–0.2 decreases by an average of 6 %, while the corresponding displacement increases by an average of 13 %, indicating that normal concrete is barely capable of carrying tensile stress and more prone to cracking after the yielding of longitudinal bars.

The lateral force-top displacement skeleton curves are presented in Fig. 12, where the lateral forces include *P*-Δ effect of axial load. By the test results, 1) Specimen H-C7–0.2 exhibits a higher peak load compared to specimen H-U0–0.2, with a slower degradation in load-bearing capacity post-peak load due to the confinement effect of the CFRP jackets. 2) The load-bearing capacity of specimen H-C7–0.4 increases with axial load, but experiences a more rapid decline after the peak load, affected by a greater *P*-Δ effect. 3) Specimen H-C7–0.2 has a slightly higher load-bearing capacity than specimen N-C7–0.2, which is mainly attributed to the tensile properties of HPFRCC. However, this contribution to the sectional bending moment is relatively limited. Similar results have been found in previous studies [7,46,47]. Also, both specimens N-C7–0.2 and H-C7–0.2 display a similar descending branch in the load-displacement curve after peak load, indicating that the effective CFRP jackets reduce the negative effects of lower shear resistance in concrete.

The moment-curvature envelope curves for all four column specimens are presented in Fig. 13. The equivalent bending moments (*M*) [48] adjusted for the *P*-Δ effect (without *P*-Δ effect) were used to evaluate the sectional compression-bending performance of the circular columns. The load-bearing capacity of specimen H-U0–0.2, lacking CFRP confinement, is observed to be the lowest and degrades rapidly after reaching peak load. In contrast, specimens H-C7–0.2 and N-C7–0.2 exhibit significantly higher load-bearing capacity, with the load remaining nearly constant and slight decreasing post peak load. This can be attributed to the secondary strengthening behavior of HPFRCC and normal concrete confined by CFRP under axial compression. The increasing axial load notably enhances the sectional load-bearing capacity of specimen H-C7–0.4, and its performance does not deteriorate appreciably even before reaching the "Collapse Prevention" (CP) limit state on drift.

The area below the moment-curvature envelope curve in Fig. 13 represents the energy dissipated during the rotation of the critical section of the column base under moment. Fig. 14 shows the energy dissipated at each level of cyclic loading in the bottom region of each column specimen within a 150 mm height range, as shown in Fig. 6. The test results reveal that specimen H-U0–0.2 exhibits the lowest rotational energy due to the lack of confinement. Specimens H-C7–0.2 and N-C7–0.2 have relatively high energy due to FRP confinement. However, the energy of specimen H-C7–0.2 is lower compared to specimen N-C7–0.2, as HPFRCC can resists tensile stress, resulting in a reduced cross-sectional curvature as observed in Fig. 13. Furthermore, the energy of specimen H-C7–0.4 is the highest due to the increased axial load.

3.4. Plastic hinge lengths and axial deformation

The flexural curvature along the height of the column can be determined by using symmetrically arranged vertical LVDTs, as shown in Fig. 6. The flexure deformations of the column specimens are mainly concentrated towards the bottom of the column, as evident from the measured curvature profile in Fig. 15. Detecting damage at the bottom of FRP-confined column specimens is difficult, so an indirect method is needed to determine the plastic hinge length through the curvature profile [49]. After reaching peak load, the sectional curvature continues to increase with deformation, but the yielding of longitudinal bars no longer extends. The plastic deformation area can be identified by locating the point where the sectional curvature exceeds the yield

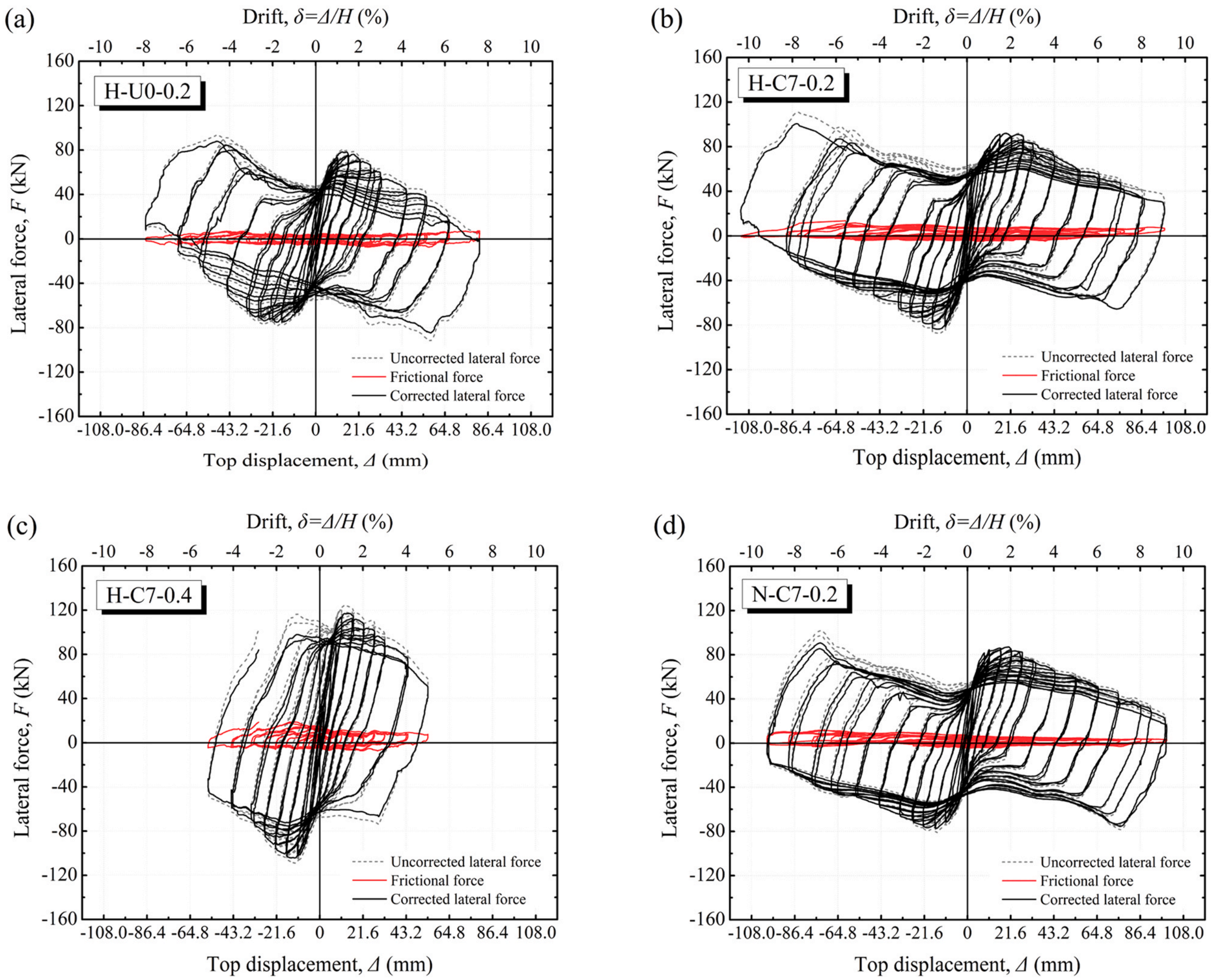

Fig. 11. Hysteresis responses for lateral force versus top displacement.

Table 7
Load results of all specimens.

Specimen	Cracking load F_{cr} (kN)			Yielding load F_y (kN)			Peak load F_p (kN)			Ultimate load F_u (kN)		
	Push	Pull	Ave.	Push	Pull	Ave.	Push	Pull	Ave.	Push	Pull	Ave.
H-U0−0.2	59.1	52.1	55.6	66.0	62.1	64.1	78.3	75.1	76.7	66.5	63.8	65.2
H-C7−0.2	—	—	—	75.1	65.8	70.5	92.0	83.0	87.5	78.2	70.5	74.4
H-C7−0.4	—	—	—	56.6	71.2	63.9	117.1	104.3	110.7	96.6	87.0	91.8
N-C7−0.2	—	—	—	77.6	63.6	70.6	87.0	76.7	81.9	73.9	64.7	69.3

Note: All loads in the table are measured results without correction for the P–Δ effect.

Table 8
Displacement results of all specimens.

Specimen	Cracking displacement Δ_{cr} (mm)			Yielding displacement Δ_y (mm)			Peak displacement Δ_p (mm)			Ultimate displacement Δ_u (mm)		
	Push	Pull	Ave.	Push	Pull	Ave.	Push	Pull	Ave.	Push	Pull	Ave.
H-U0−0.2	5.4	5.4	5.4	6.9	7.1	7.0	15.4	19.6	17.5	27.4	33.2	30.3
H-C7−0.2	—	—	—	8.7	6.5	7.6	19.3	16.4	17.9	36.6	28.2	32.4
H-C7−0.4	—	—	—	4.9	4.9	4.9	14.6	14.3	14.5	28.8	26.1	27.5
N-C7−0.2	—	—	—	7.1	7.0	7.0	20.6	20.0	20.3	32.8	33.8	33.3

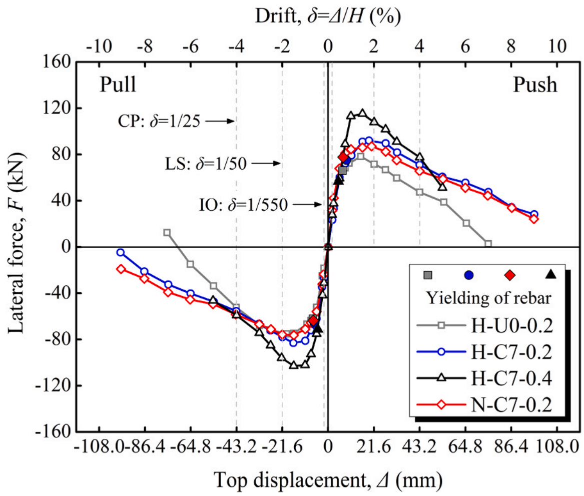

Fig. 12. Lateral force-displacement skeleton curves.

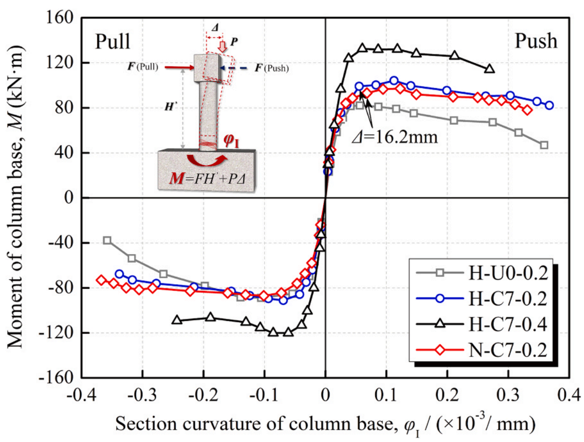

Fig. 13. Moment-curvature envelope curves.

curvature at peak load. In Fig. 15, the plastic hinge zone is approximately determined based on the limited number of LVDTs, serving as the upper limit of the plastic hinge length. Among the three specimens with an axial load ratio of 0.2, the unconfined specimen H-U0–0.2 exhibits a plastic hinge length of approximately 22–27 % of the total height, equivalent to an average height of around 265 mm (about 1.1 times the diameter of column, *D*). The CFRP-confined specimens H-C7–0.2 and N-C7–0.2 have plastic hinge lengths of around 20 % of the total height, translating to an average height of around 215 mm (about 0.9*D*). As for the specimen H-C7–0.4 with an axial load ratio of 0.4, the plastic hinge length is estimated to be approximately 28–32 % of the total height, which corresponds to around 325 mm (about 1.35*D*). This observation that plastic hinge length increases with axial load ratio is consistent with the findings of Pam and Ho [49].

The average axial deformation of the columns under both axial and lateral loads can be measured by LVDT-11 and LVDT-12, as shown in Fig. 16. Before reaching peak load, both CFRP-confined column specimens (H-C7–0.2 and N-C7–0.2) with an axial load ratio of 0.2 exhibit a greater variation in axial deformation between lateral displacements from 0 to the maximum, whereas the CFRP-confined column (H-C7–0.4) with an axial load ratio of 0.4 shows a smaller variation.

3.5. Strain distribution of CFRP

The confined cement-based material in the column experiences lateral expansion caused by axial compression and bending moment, resulting in tensile strain in the CFRP jackets. As the compressive stress in the cement-based material increases, the tensile strain in the CFRP also increases. The maximum axial compressive stress in the cement-based material is theoretically at the critical section at the base of the cantilever column. However, due to material degradation and non-uniform forces, the actual maximum tensile strain in the CFRP occurred near the bottom of the column. In specimens H-C7–0.2 and N-C7–0.2, the largest lateral strain in the CFRP is observed at Section-1, while for specimen N-C7–0.4, it occurs at Section-2, as shown in Fig. 17.

The strain distribution in the CFRP of the three confined specimens under push loading shows clear asymmetry. Tensile strains on the side of the column section experiencing higher compressive stress (i.e., A1H or A2H, on the left side of the section) are notably greater than those on the side with tensile stress or lower compressive stress (i.e., E1H or E2H, on the right side of the section). At the yield state, the maximum tensile strains in the CFRP of all three specimens are lower than the lateral strains corresponding to the peak stress of the unconfined cement-based materials (i.e., 1500 μ*ε* for HPFRCC and 706 μ*ε* for concrete), indicating a lower confinement pressure exerted by the CFRP. However, upon reaching the peak load, the maximum tensile strain in the CFRP exceeds the lateral strain corresponding to the peak stress of the unconfined cement-based materials. As the drift increased from 2 % to 4 %, the

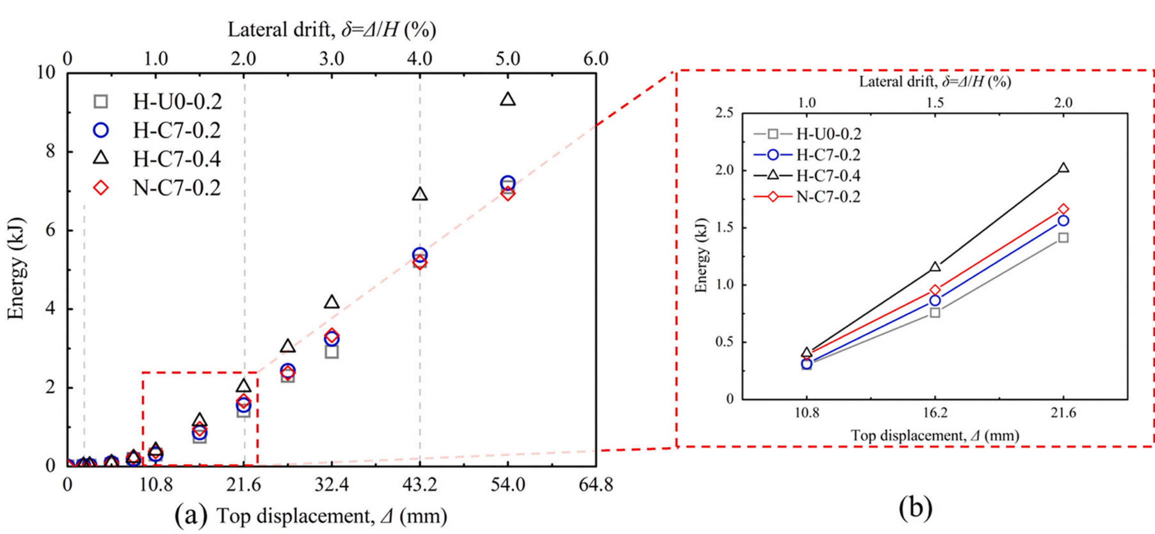

Fig. 14. Energy dissipation.

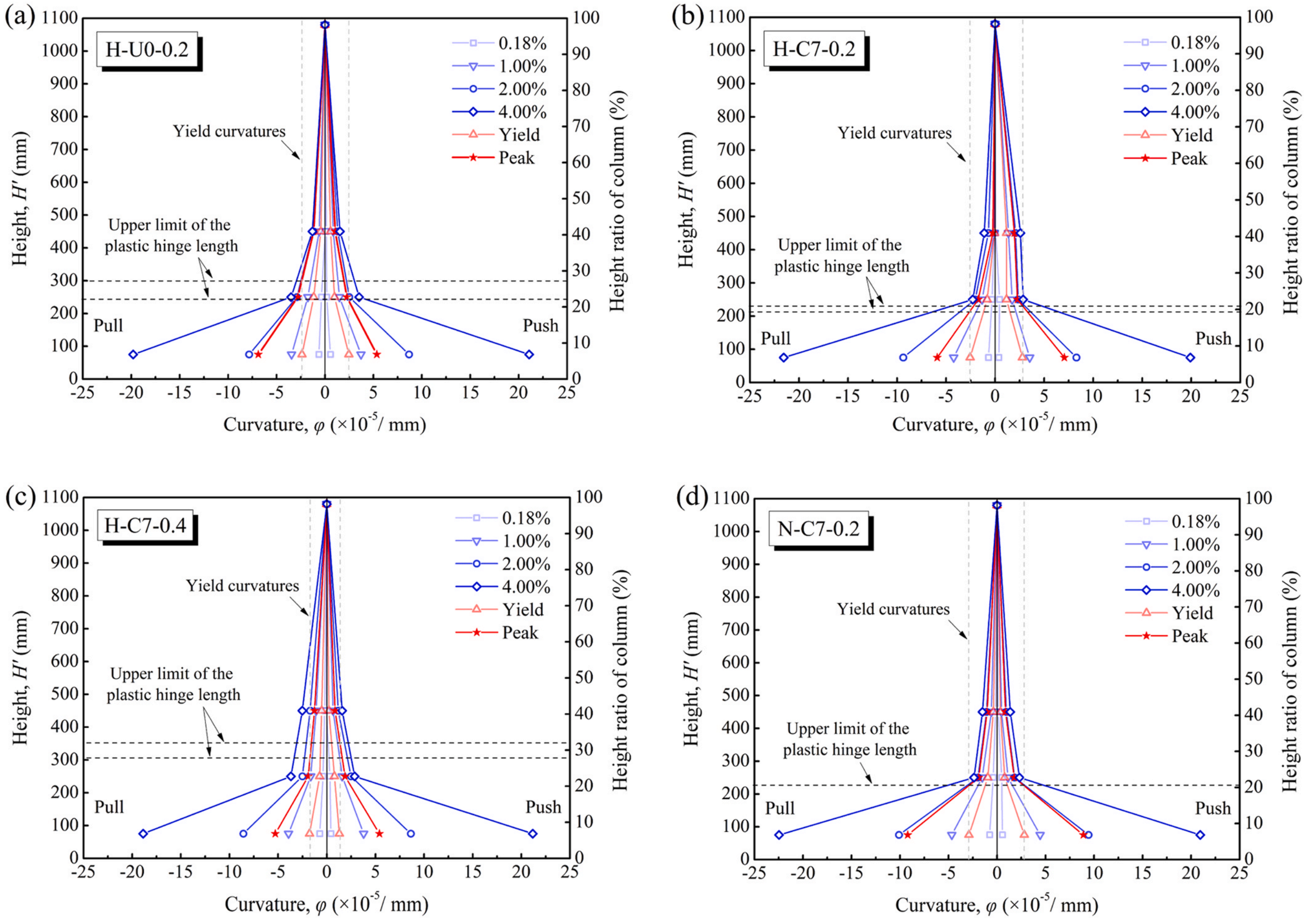

Fig. 15. Measured curvature profile and plastic hinge length of column.

maximum tensile strain in the CFRP significantly rose, revealing a stronger confinement effect. At a drift of 4 %, the maximum tensile strain reached 25.6 %, 20.8 % and 39.7 % of the ultimate tensile strain of CFRP for specimens H-C7–0.2, N-C7–0.2, and H-C7–0.4, respectively. Furthermore, in Figs. 17**a** and 17**b**, it is evident that the lateral tensile strain of CFRP for specimen H-C7–0.2 is greater than that of specimen N-C7–0.2 both at peak load and at a drift of 4 %. This implies that the localized lateral expansion of concrete under compression is more prominent due to the brittleness of concrete at fracture.

At peak load, the CFRP on the rightmost section of specimens H-C7–0.2 and N-C7–0.2 exhibited a lateral strain of approximately 1000 $\mu\varepsilon$, as seen in Figs. 17**a** and 17**b**. However, specimen H-C7–0.4, which was subjected to a larger axial load, demonstrated a lateral strain close to zero (Fig. 17**c**). This unexpected result is likely attributed to axial deformation. Specimens with lower axial loads were more prone to the tensile yielding of longitudinal bars and cracking of cement-based materials. As a result, during cyclic loading, the longitudinal bars experienced increased axial and buckling deformations, leading to greater lateral expansion of the CFRP. The inference is supported by the average measured axial deformation at peak load, as indicated in Fig. 16.

4. Conclusions

Based on the quasi-static cyclic tests conducted in this study on the CFRP-confined steel-reinforced HPFRCC circular columns, the following conclusions can be drawn:

1) The main contributions of this research were the development of a novel seismic column design and the examination of its cyclic behavior utilizing specifically devised test methods and equipment. The findings indicated that the CFRP-confined steel-reinforced HPFRCC circular column specimen exhibited improved sectional compression-bending performance due to the tensile strain-hardening ability of HPFRCC and the axial compression strengthening effect provided by CFRP confinement.

2) Compared to unconfined columns, HPFRCC columns confined with CFRP exhibited higher yield and peak loads, along with greater yield and ultimate displacements. This indicated that FRP confinement effectively improved the load-bearing capacity of columns, delayed the decrease in load post-peak, and even demonstrated secondary strengthening behavior in the sectional compression-bending performance.

3) The column specimen made of ductile HPFRCC exhibited a greater yielding displacement and peak load compared to the column made of brittle concrete. This could be attributed to the superior tensile ductility of HPFRCC. However, the tensile strain hardening properties of HPFRCC had only a limited effect on enhancing the sectional compression-bending performance of the column under FRP confinement.

4) As the axial load increased, the longitudinal bars in the column yielded earlier under compression, resulting in a substantial decrease in both the yield displacement and the displacement at peak load. The peak load also significantly increased, while the compression-bending performance remained roughly stable until reaching the collapse prevention (CP) limit state. This behavior was attributed to the axial compression strengthening of HPFRCC under the confinement effect of FRP.

Further investigation and validation are necessary to confirm the above findings, as the sample size is limited.

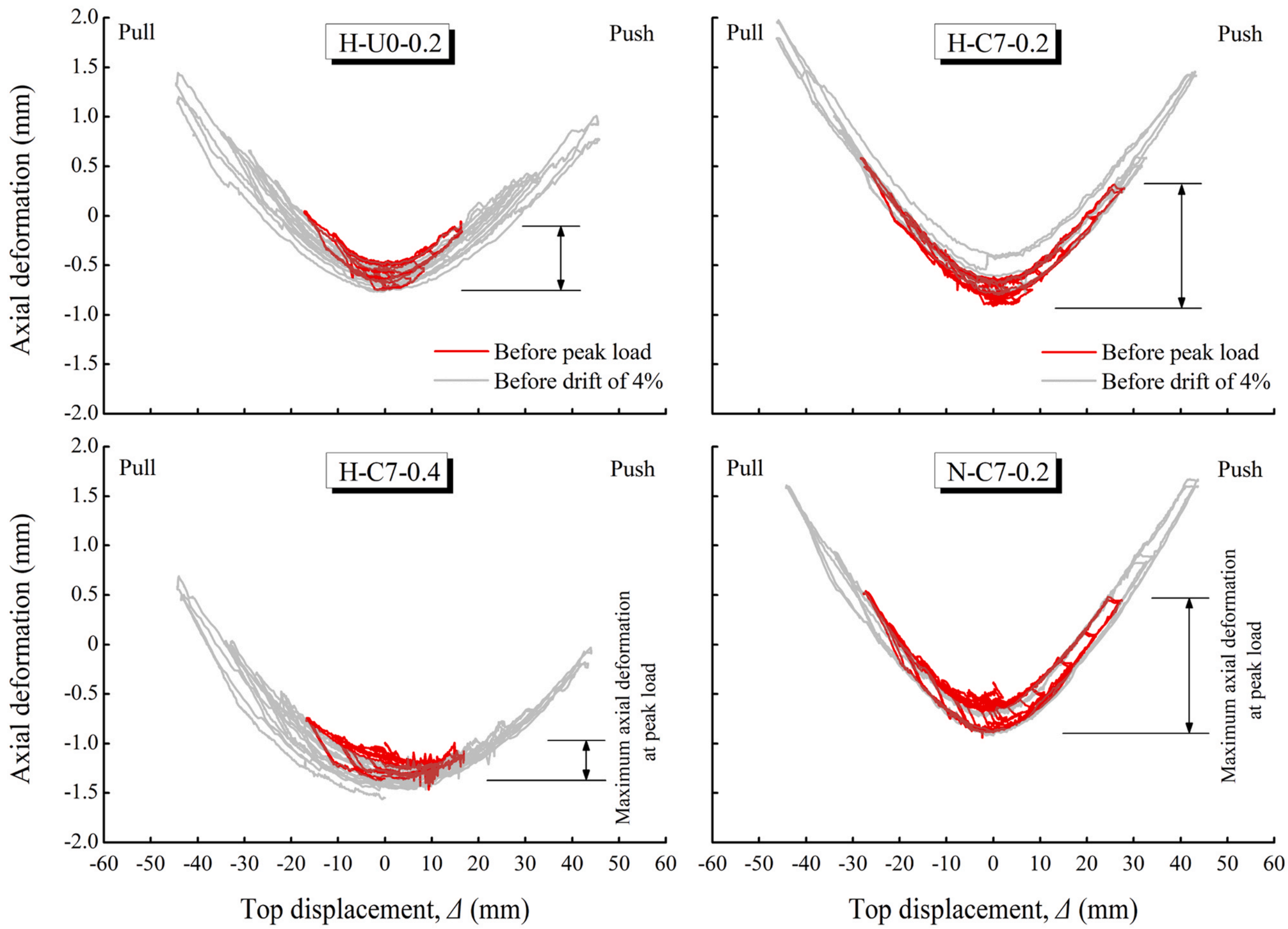

Fig. 16. Axial deformation of the columns.

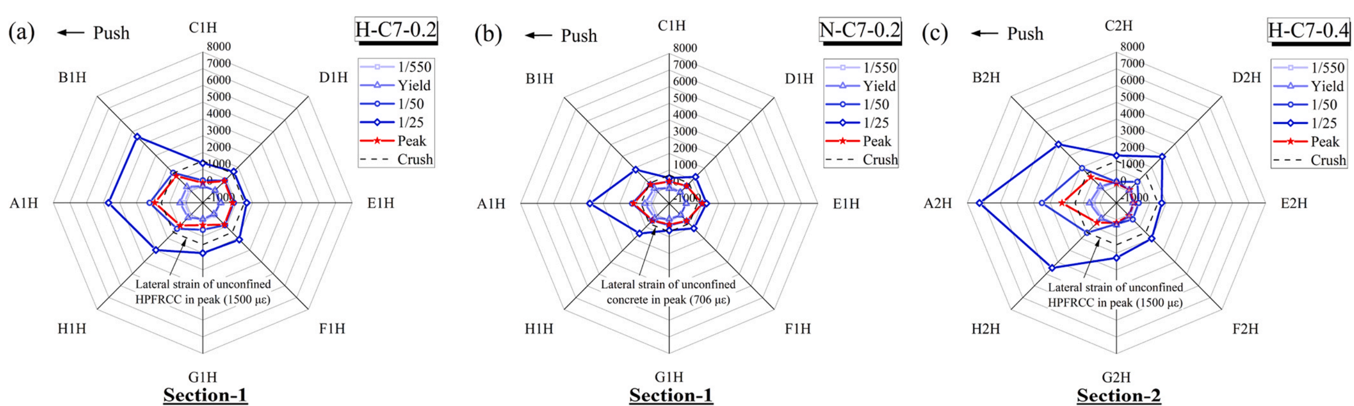

Fig. 17. Strain distribution of CFRP (Unit: με).

CRediT authorship contribution statement

Zheng Dang: Conceptualization, Methodology, Investigation, Data Curation, Writing – original draft, Writing – review & editing. **Peng Feng**: Conceptualization, Supervision. **Saravath Suong**: Investigation, Visualization. **Liyun Tang**: Writing – review & editing.

Declaration of Competing Interest

The authors declare that they have no known competing financial interests or personal relationships that could have appeared to influence the work reported in this paper.

Data availability

All data, models, and code generated or used during the study appear in the submitted article.

Acknowledgments

This study is supported by the National Natural Science Foundation of China [Grant No. 51708331] and the China Postdoctoral Science Foundation [Grant No. 2017M610903]. The authors are grateful to Dr. Li Hu of Tsinghua University for her assistances with this experiment.

References

[1] Naaman A.E. Half a century of progress leading to ultra-high performance fiber reinforced concrete: part 1-overall review. Proceedings of 2nd International RILEM Conference on Strain Hardening Cementitious Composites. Rio de Janeiro: RILEM Publications SARL; 2011:17–26.
[2] Paulay T, Priestley MJN. Seismic design of reinforced concrete and masonry buildings. New York: John Wiley & Sons; 1992.
[3] Li VC, Leung CKY. Steady state and multiple cracking of short random fiber composites. J Eng Mech 1992;188(11):2246–64.
[4] Li VC, Wu HC. Conditions for pseudo strain hardening in fiber reinforced brittle matrix composites. Appl Mech Rev 1992;45(8):390–8.
[5] Naaman AE, Paramasivam P, Balazs G, Bayasi ZM, Eibl J, Erdelyi L, et al. Reinforced and prestressed concrete using HPFRCC matrices. High Performance Fiber Reinforced Cement Composites. RILEM Proc, 31. London: E&FN Spon; 1996. p. 291–347.
[6] Cho CG, Kim YY, Feo L, Hui D. Cyclic responses of reinforced concrete composite columns strengthened in the plastic hinge region by HPFRC mortar. Compos Struct 2012;94:2246–53.
[7] Xu L, Pan J, Chen J. Mechanical behavior of ECC and ECC/RC composite columns under reversed cyclic loading. J Mater Civ Eng 2017;29(9):04017097.
[8] Li X, Wang J, Bao Y, Chen G. Cyclic behavior of damaged reinforced concrete columns repaired with high-performance fiber-reinforced cementitious composite. Eng Struct 2017;136:26–35.
[9] Fischer G, Li VC. Effect of matrix ductility on deformation behavior of steel reinforced ECC flexural members under reversed cyclic loading conditions. ACI Struct J 2002;99(6):781–90.
[10] Fischer G, Li VC. Influence of matrix ductility on tension stiffening behavior of steel reinforced engineering cementitious composites (ECC). ACI Struct J 2002;99(6): 104–11.
[11] Kesner K, Billington SL. Investigation of infill panels made from engineered cementitious composites for seismic strengthening and retrofit. J Struct Eng 2005; 131(11):1712–20.
[12] Kesner KE, Billington SL, Douglas KS. Cyclic response of highly ductile fiber-reinforced cement-based composites. ACI Mater J 2003;100(5):381–90.
[13] Kesner K.E., Billington S.L. Tension, compression and cyclic testing of engineered cementitious composite materials. Technical Report MCEER-04–0002. New York: Cornell University; 2004.
[14] Ozbakkaloglu T, Lim JC, Vincent T. FRP-confined concrete in circular sections: review and assessment of stress-strain models. Eng Struct 2013;49:1068–88.
[15] Liu J, Teng Y, Zhang Y, Wang X, Chen YF. Axial stress-strain behavior of high-strength concrete confined by circular thin-walled steel tubes. Constr Build Mater 2018;177:366–77.
[16] Baduge SK, Mendis P, Ngo T, Portella J, Nguyen K. Understanding failure and stress-strain behavior of very-high strength concrete (>100 MPa) confined by lateral reinforcement. Constr Build Mater 2018;189:62–77.
[17] Chin CL, Ma CK, Tan JY, Ong CB, Awang AZ, Omar W. Review on development of external steel-confined concrete. Constr Build Mater 2019;211:919–31.
[18] Mirmiran A, Shahawy M. Dilation characteristics of confined concrete. Mech Cohesive-Frict Mater 1997;2:237–49.
[19] Spoelstra MR, Monti G. FRP-confined concrete model. J Compos Constr 1999;3(3): 143–50.
[20] Seible F, Priestley MJN, Hegemier GA, Innamorato D. Seismic retrofit of RC columns with continuous carbon fiber jackets. J Compos Constr 1997;1(2):52–62.
[21] Ye LP, Zhang K, Zhao SH, Feng P. Experimental study on seismic strengthening of RC columns with wrapped CFRP sheets. Constr Build Mater 2003;17:499–506.
[22] Gu DS, Wu G, Wu ZS, Wu YF. Confinement effectiveness of FRP in retrofitting circular concrete columns under simulated seismic load. J Compos Constr 2010;14 (5):531–40.
[23] Wang D, Wang Z, Smith ST, Yu T. Seismic performance of CFRP-confined circular high-strength concrete columns with high axial compression ratio. Constr Build Mater 2017;134:91–103.
[24] Dang Z, Feng P, Yang JQ, Zhang Q. Axial compressive behavior of engineered cementitious composite confined by fiber-reinforced polymer. Compos Struct 2020;243:112191.
[25] Yuan WY, Han Q, Bai YL, Du XL, Yan ZW. Compressive behavior and modelling of engineered cementitious composite (ECC) confined with LRS FRP and conventional FRP. Compos Struct 2021;272:114200.
[26] Li S, Chan TM, Young B. Compressive behavior and analysis-oriented model of FRP-confined engineered cementitious composite columns. Eng Struct 2022;270: 114869.
[27] Yuan W, Han Q, Bai Y, Song Y, Zhang Q. Size effect on compressive behavior of FRP-confined engineered cementitious composites (ECC). Constr Build Mater 2022; 348:128610.
[28] Jiang J, Cui Y, Han Z. Experimental study and analysis-oriented model of PET FRP confined ECC cylinders under monotonic axial compression. Eng Struct 2023;280: 115610.
[29] Zeng JJ, Liang QJ, Cai WJ, Liao J, Zhou JK, Zhu JY, et al. Strengthening RC square columns with UHP-ECC section curvilinearization and FRP confinement: concept and axial compression tests. Eng Struct 2023;280:115666.
[30] Lai MH, Hanzic L, Ho JCM. Fillers to improve passing ability of concrete. Struct Concr 2019;20(1):185–97.
[31] Lai MH, Wu KJ, Cheng X, Ho JCM, Wu JP, Chen JH, et al. Effect of fillers on the behaviour of heavy-weight concrete made by iron sand. Constr Build Mater 2022; 332:127357.
[32] GB 50010–2010. Code for design of concrete structures. Beijing, China: China Architecture & Building Press; 2015.
[33] Vincent T, Ozbakkaloglu T. Influence of overlap configuration on compressive behavior of CFRP-confined normal- and high-strength concrete. Mater Struct 2016; 49:1245–68.
[34] GB/T 228.1–2021. Metallic materials-Tensile testing-Part 1: Method of test at room temperature. Beijing, China: Standards Press of China; 2021.
[35] ASTM D3039/D3039M-00. Standard test method for tensile properties of polymer matrix composite materials. West Conshohocken, PA: ASTM International; 2000.
[36] GB/T 3354-2014. Test method for tensile properties of orientation fiber reinforced polymer matrix composite materials. Beijing, China: Standards Press of China; 2014.
[37] Lam L, Teng JG. Ultimate condition of fiber reinforced polymer-confined concrete. J Compos Constr 2004;8(6):539–48.
[38] GB/T 50081–2019. Standard for test methods of concrete physical and mechanical properties. Beijing, China: China Architecture & Building Press; 2019.
[39] GB 50011-2010. Code for seismic design of building. Beijing: China: China Architecture & Building Press; 2016.
[40] FEMA 356. Prestandard and commentary for the seismic rehabilitation of buildings. Washington DC: Federal Emergency Management Agency; 2000: 6–19-6–55.
[41] Zhang B, Teng JG, Yu T. Experimental behavior of hybrid FRP-concrete-steel double-skin tubular columns under combined axial compression and cyclic lateral loading. Eng Struct 2015;99:214–31.
[42] Yao LZ, Wu G. Fiber-element modeling for seismic performance of square RC bridge columns retrofitted with NSM BFRP bars and/or BFRP sheet confinement. J Compos Constr 2016;20(4):04016001.
[43] Feng P, Cheng S, Yu T. Seismic performance of hybrid columns of concrete-filled square steel tube with frp-confined concrete core. J Compos Constr 2018;22(4): 04018015.
[44] Xiao Y. Experimental methods for seismic simulation of structural columns: State-of-the-art review and introduction of new multiuse structural testing system. J Struct Eng 2019;145(3):04018269.
[45] Liu L, Pan P, Wang H, Feng P, Zhao M. Development and application of friction force measurement device for compression-shear tests. J Build Struct 2019;40(6): 133–9.
[46] Billington SL, Yoon JK. Cyclic response of unbonded posttensioned precast columns with ductile fiber-reinforced concrete. J Bridge Eng 2004;9(4):353–63.
[47] Xu Y, Jia Y, Tong Z, Shivahari S. Cyclic loading test for concrete bridge columns integrated with ECC segment at the plastic zone. Eng Struct 2021;246:112985.
[48] Sharbatdar MK, Saatcioglu M. Seismic design of FRP reinforced concrete structures. Asian J Appl Sci 2009;2(3):211–22.
[49] Pam HJ, Ho JCM. Length of critical region for confinement steel in limited ductility high-strength reinforced concrete columns. Eng Struct 2009;31:2896–908.